RSC Advances

ROYAL SOCIETY OF CHEMISTRY

PAPER

View Article Online
View Journal | View Issue

Cite this: *RSC Adv.*, 2026, **16**, 14107

Harnessing synergistic effects in porous carbon/Co-ZnO heterojunction for enhanced visible-light photocatalytic removal of bisphenol A

Shisak Sharma, Raplang Steven Umdor, Imotila T. Longchar, Partha Pratim Gogoi, Soremo L. Ezung and Dipak Sinha *

Endocrine-disrupting contaminants, particularly bisphenol A (BPA), are prevalent in aquatic environments, posing severe ecological and health risks that demand efficient remediation strategies. Photocatalysis has emerged as a promising enhanced oxidation technology for the mitigation of such recalcitrant organic pollutants. Herein, we report the hydrothermal synthesis of a CCAC/Co-ZnO nanocomposite, achieved by anchoring cobalt doped ZnO nanoparticles onto activated carbon obtained from Croton caudatus biomass. Characterization studies (XRD, SEM, EDS, HR-TEM, XPS, BET surface area, PL and UV-Vis DRS) validated the optimized nanostructure, and photocatalytic evaluations showed 99.67% BPA breakdown within 60 min under visible light irradiation at optimal conditions. The reaction obeyed pseudo-first-order kinetics ($t_{1/2}$ of 12.6 min and k_{ap} of 0.055 min^{-1}), dominated by hydroxyl radicals (•OH), and photogenerated holes (h^+) as primary reactive oxygen species (ROS). LC-MS identified intermediates enabled proposal of a plausible BPA degradation pathway, while reusability studies showed 77.63% efficiency over five cycles, confirming excellent photostability and reusability. Moreover, DFT calculations elucidated improved ROS generation mechanisms, providing mechanistic insights into the degradation processes. These findings provide a viable strategy for designing biomass-derived, visible-light-responsive photocatalysts for sustainable environmental remediation applications.

Received 24th January 2026
Accepted 10th March 2026

DOI: 10.1039/d6ra00641h

rsc.li/rsc-advances

1. Introduction

In recent times, the widespread occurrence of endocrine-disrupting chemicals (EDCs) in the aquatic environment has become a global concern. Bisphenol A (BPA) is one of the commonly detected EDCs in groundwater, surface water, industrial effluents, and landfill leachate. Its presence is primarily attributed to its wide-ranging application as a precursor in the production of epoxy resins, polycarbonate plastics and other polymers (*e.g.*, rubber antioxidants, food packaging containers, dental sealants, PCV pipes, and other fine chemical materials).[1–3] BPA is constituted of two phenolic rings joined by an acetone-derived bridge, from which its nomenclature is derived ('A' denotes acetone).[4] According to reports, 27 million tonnes of polymers containing BPA are produced globally each year, with 60% (approx.) of the world's BPA consumption coming from Asian countries.[5,6] Owing to its extensive use, BPA is ubiquitously released in the environment, posing adverse effects on both human health and the ecosystem. BPA also poses other health concerns, due to its potential carcinogenic and genotoxic implications.[7,8] Studies have indicated that exposure to BPA may promote the growth of cancer cells, especially in the tissues of the breast and prostate. Beyond this, BPA has been associated with various other health issues, including infertility, obesity, and developmental abnormalities.[9–11] The substantial toxicity of BPA is largely due to its unique physicochemical properties. These include high solubility in water (about 200 mg L^{-1} @ 25 °C), chemical stability, and resistance to biodegradation, allowing it to persist in aquatic environments even at very low concentrations (pM or nM).[12,13] Consequently, several nations and regions, including the European Union, Sweden, Canada, United States, Norway, India and China, have banned the usage of BPA.[14] Similarly, the USEPA has also included this compound on the Drinking Water Contaminant Candidate List 5.[15] As a result, there is an urgent need to develop highly efficient strategies for BPA removal from aqueous media.

To address the growing concern pertaining to emerging organic substances (*e.g.*, BPA) in wastewater, several methods of treatment have been investigated, including chemical oxidation, biological treatment, adsorption, membrane separation, electro-Fenton processes and photocatalysis.[16–18] Among these, heterogeneous photocatalysis has emerged as a promising approach in advanced oxidation processes (AOPs) over other conventional methods due to its mild operating conditions, eco-friendliness, reusability, long-term stability, high degradation efficiency, lack of secondary pollutants and wide

Department of Chemistry, Nagaland University, Lumami-798627, Nagaland, India. E-mail: dipaksinha@gmail.com

applications.[19,20] In AOPs, the absorption of UV or visible radiation by a semiconductor material promotes an electron from the valence band (VB) to the conduction band (CB), leading to the generation of an electron–hole (e^-/h^+) pair. The photogenerated holes in the VB exhibit significant oxidative potential, enabling them to combine with water molecules or surface-bound hydroxyl groups to produce hydroxyl radicals ($^{\bullet}OH$), whilst the conduction band electrons can convert molecular oxygen to superoxide radicals ($^{\bullet}O_2^-$).[21–23] These reactive oxygen species (ROS) initiate a series of redox reactions that lead to the degradation of organic pollutants, converting them into complete mineralized of byproducts such as carbon dioxide (CO_2) and water.[24,25] For instance, Rajeshwari *et al.*[26] developed a g-C_3N_4 quantum dot-modified α-MoO_3 nanohybrid and demonstrated its effectiveness in the visible-light irradiation for photocatalytic degradation of *p*-chlorophenol and rifampicin.

Numerous studies have reported the use of semiconductor photocatalysts such as ZnO, TiO_2, CdO, Fe_3O_4, CuO, and CdS for the effective degradation of organic pollutants.[27–29] Among them, ZnO has attracted considerable interest due to its excellent photochemical stability, high electron mobility (300 $cm^2 V^{-1} s^{-1}$), non-toxicity, strong exciton binding energy (60 meV), favorable optical properties and cost-effectiveness.[30] Nevertheless, ZnO suffers from intrinsic limitations: a wide band gap (3.37 eV), low photon absorption, poor separation, rapid recombination of photogenerated electron–hole pairs, that restrict their catalytic activity under visible-light irradiation.[31] To overcome these challenges, extensive efforts have been focused on tuning the electronic and optical properties of ZnO through doping with transition metals (*e.g.*, Co, Ni, Mn, Fe, Cu, *etc.*).[32,33] The incorporation of these dopants introduces intermediate energy levels within the ZnO band structure, effectively narrowing the band gap and extending its light absorption into the visible range.[34] For example, Lu *et al.* (2011) synthesized Co-doped ZnO nanorods *via* a hydrothermal method and reported a 93% degradation efficiency of 58 μM alizarin red dye within 60 min under visible-light irradiation.[35] Similarly, Ullah and coauthors observed enhanced discolouration of methylene blue using Mn-doped ZnO nanoparticles.[36] The photocatalytic degradation of rhodamine B under visible light was significantly improved by Ni-doped ZnO nanorods, as studied by Zhao *et al.* (2011).[37] Cobalt (Co) is widely recognized as a highly compatible dopant for ZnO, supported by the Lattice Compatibility Theory.[38] Its high electron-donating ability, resistance to photo-corrosion, strong surface adsorption, visible surface plasmon resonance, and excellent solubility within the ZnO lattice contribute to its efficacy as a dopant.[39,40]

Another problem faced with ZnO nanoparticles is their vulnerability to photo-induced deterioration in aqueous conditions, as well as their tendency to aggregate, especially at higher concentrations, which complicates post-reaction separation and restricts their reusability.[41,42] One practical and innovative technique to overcome the limitations of conventional photocatalyst involves the use of biomass-derived carbonaceous materials to form heterojunction composites.[43] Carbon-based nanostructures offer numerous benefits, such as high porosity, tunable surface functions, large BET surface area, high stability and good recycling characteristics, making them appropriate as support material for photocatalysts. In addition, transforming biomass waste into activated carbon (AC) is considered an environmentally beneficial solution because it not only tackles solid waste management issues yet also lowers the cost of raw material procurement.[44,45] In this context, ZnO nanoparticle is immobilized on high-surface-area carbonaceous supports, which promote uniform dispersion of the photocatalyst, inhibit nanoparticle agglomeration, and enhance overall photocatalytic activity during adsorption-degradation pathways.[46,47] The superior performance of these heterogeneous photocatalyst is primarily attributed to the synergistic interactions formed between the porous carbon matrix and semiconductor interface. For instance, Faisal *et al.* (2021) developed a novel biomass-derived activated carbon (AC)@ZnO/SnO_2 composite, which demonstrated outstanding visible-light-driven activity, achieving 94.6% degradation of the antibiotic linezolid.[48] In another study, Shanmugam *et al.* (2024) successfully synthesised carbon aerogel-supported CA/ZnS–Ag composites using low-cost biomass precursors *via* hydrothermal process and reported 98.64% degradation within 150 min.[49] This integrated approach represents a promising and sustainable strategy for the removal of BPA from wastewater.

Despite these developments, there is still a significant gap in the development of visible-light-active photocatalysts that are designed to degrade BPA. Although ZnO-based photocatalysts have been rigorously investigated for the degradation of organic contaminants, the integration of Co-doped ZnO with biomass derived AC for degradation of BPA under visible light illumination remains unexplored. Moreover, to the best of our knowledge, there has been no report of using *croton caudatus* biomass as a carbon precursor in photocatalytic applications.

Therefore, the present work aims to synthesize Co-doped ZnO photocatalyst immobilized on biomass derived AC (porous carbon) *via* hydrothermal synthesis route. The resultant heterojunction photocatalyst were systematically characterized and studied. The performance of porous carbon/Co-ZnO nanocomposite was assessed under visible light irradiation for the degradation of BPA. Furthermore, multiple-cycle experiments were conducted to evaluate the stability and reusability of the photocatalyst. Radical scavenging assays were used to determine the primary reactive species involved in the degradation mechanism. Additionally, a plausible degradation pathway was postulated based on the identification of intermediate products obtained through liquid chromatography-mass spectrometry (LC-MS) analysis.

2. Experimental section

2.1. Materials

Cobalt nitrate hexahydrate ($Co(NO_3)_2 \cdot 6H_2O$, MW: 291.03 g mol^{-1}, ≥ 99.90%), zinc oxide (ZnO, MW: 81.38 g mol^{-1}, ≥ 99%), bisphenol A (BPA, MW: 228.29 g mol^{-1}, ≥ 99%) were purchased from the Sigma-Aldrich, India. Ethanol, HCL and NaOH were procured from SRL, India. The chemical structure and properties of BPA are shown in Table S1. The chemicals obtained were of analytical grade and used without further treatment. Double

distilled water (DDW) from Milli-Q system (18.2 MΩ cm) was utilized throughout all testing experiments.

2.2. Preparation of porous carbon

The croton caudatus biomass collected from the University Campus (26°13′29.60″ N | 94°28′35.0″ E), was used as the primary raw material. The entire plant was employed to produce activated carbon. The collected biomass was cut into small fragments and thoroughly rinsed with DDW to eliminate surface contaminants and residual materials. The biomass was then oven-dried at 105 °C for 24 h to remove the moisture content. The processed biomass was subsequently used for the preparation of *Croton caudatus* activated carbon (CCAC). The overall yield of porous carbon obtained from the raw biomass was around 32.5%. Details on the synthesis and characterisation of CCAC have been described in our previous paper.[50]

2.3. Synthesis of CCAC/Co-ZnO nanocomposite

The CCAC/Co-ZnO nanocomposite was created *via* a hydrothermal approach. Initially, 0.15 g of ZnO nanoparticles were gradually added to 100 mL of cobalt nitrate solution (1 g) while continuously stirring for 30 min. Subsequently, 0.3 g of synthesised CCAC was gently added to the resultant mixture, which was then ultrasonically dispersed for 1 hour to achieve uniform distribution. The resulting suspension was then transferred into a Teflon-lined autoclave and subjected to hydrothermal treatment at 150 °C for 16 hours. After completion, the product was thoroughly washed using centrifugation until a neutral pH was achieved and then dried at 65 °C for 12 hours. The synthesised nanocomposite was further explored to assess BPA degradation. Fig. 1 depicts a schematic illustration of the preparation procedure for the synthesized nanocomposite.

2.4. Characterization techniques

Several advanced characterisation techniques were used to analyse the CCAC/Co-ZnO nanocomposite. These include X-ray diffraction (XRD, PANalytical, Empyrean, CuKα radiation), Transmission electron microscopy (TEM, 2100F, JOEL), Scanning electron microscopy (SEM, JSM-6360, JEOL), accompanied by energy dispersive X-ray spectroscopy (EDX), X-ray photoelectron spectroscopy (XPS, M/s Physical Electronics, PHI 5000 versa probe III) Photoluminescence analysis (PL, Horiba Fluoromax4CP spectrofluorometer, 150 W Xenon Lamp), Diffuse reflection spectrophotometer (DRS, Shimadzu, and wavelength), BET surface area analyzer (Quantachrome AutosorbiQ Station 1 at 77 K), LC-MS spectrophotometer (INKAR, Expression-S), Total organic carbon, (TOC, Shimadzu Model 5000A). The batch equilibration method was employed to determine the zero-point charge (pH_{zpc}) of the photocatalyst.[43]

2.5. Photocatalytic degradation experiments

The photocatalytic degradation of BPA was carried out inside a photocatalytic reactor enclosed within a light-shielded black box with dimensions of 63 × 44 × 44 cm. In this experiment, the catalytic degradation of BPA was performed over a period of 60 min under visible light emitted from a 350 W high-pressure Hg lamp (wavelength 520 nm) positioned 10 cm above the reactor to illuminate the reaction mixture. Typically, 50 mL of BPA solution (20 mg L^{-1}) and required load of the photocatalyst were introduced and agitated for 30 min in the absence of light to attain adsorption–desorption equilibrium inside the reaction system. During the reaction, 3.5 mL of the solution was extracted every 10 min, and the concentration of the solution was determined at 276 nm using a UV-Vis spectroscopy analysis (Lambda-365). All tests were repeated three times and averages were reported to assure data quality. Eqn (1) was used to calculate the degradation rate of BPA.

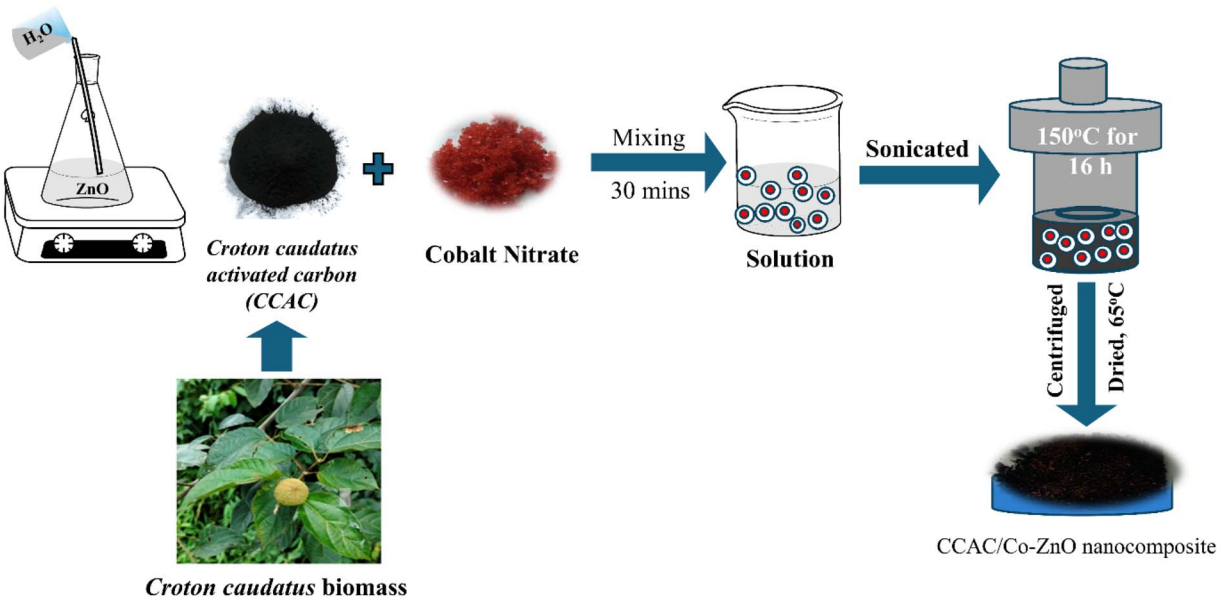

Fig. 1 Scheme for preparation of the *Croton caudatus* activated carbon (CCAC)/Co-ZnO photocatalyst.

$$\text{Degradation rate } (\%) = (1 - C_t/C_0) \times 100 \quad (1)$$

where C_0 and C_t are the concentrations (mg L^{-1} or ppm) of BPA before and after the photocatalytic process at varying irradiation intervals, respectively.

The schematic representation of the experimental setup used for the visible light-driven photocatalytic process is presented in Fig. S1 in SI.

3. Results and discussion

3.1. Characteristics of CCAC/Co-ZnO

X-ray diffraction (XRD) analysis was performed to examine the crystal lattice structure of the synthesized nanocomposite as shown in Fig. 2a. The intensity peak at $2\theta = 26.5°$ represents the (1 0 0) planes of hexagonal graphitised carbon (ICDD 08-0415).[51] The diffraction peaks at 2θ values of 31.73° (100), 34.36° (002), 36.21° (101), 47.47° (102), 56.53° (110), 62.75° (103), 67.85° (112) and 68.99° (201) attribute to the hexagonal wurtzite crystal structure of ZnO (ICDD 80-0074).[52] The observed diffraction peaks are in good agreement with previously reported literature.[53,54] Despite the incorporation of Co^{2+} ions into the Zn^{2+} sites within the ZnO lattice, no alteration in the crystalline structure of the ZnO was observed.[55] The Scherrer equation was used to calculate the average crystallite size (D) of the synthesised sample. It is represented as follows:

$$D = \frac{0.9\lambda}{\beta \ \mathrm{Cos}\theta}$$

where λ indicate the wavelength of X-ray radiation, θ is the glancing angle, and β is the full width at half-maximum (FWHM). Evidently, the D value for CCAC/Co-ZnO was determined to be 18.24 nm using the FWHM of its most strong diffraction peaks. The XRD pattern of pristine CCAC is provided in Fig. S2, suggesting the amorphous nature of CCAC.

FT-IR analysis indicated the existence of various surface functional groups on the CCAC/Co-ZnO nanocomposite and CCAC as depicted in Fig. 2b. The extensive absorption band centered at 3440–3444 cm^{-1} is indicative of O–H stretching vibrations from surface hydroxyl groups, physisorbed water, and oxygen-containing functional groups present in CCAC. The inclusion of Co–ZnO results in the further broadening and intensification of the O–H band, signifying stronger hydrogen bonding and improved surface hydroxylation in the composite. The peak at around 1632 cm^{-1} is attributed to the H–O–H bending vibration of adsorbed water molecule.[56] The intensity variations within the 1500–1600 cm^{-1} range validate the interactions between the carbon matrix and metal oxides. Notably, the formation of new absorption bands in the 500–700 cm^{-1} range corresponds to Zn–O and Co–O stretching vibrations, offering the successful integration of Co–ZnO nanoparticles onto the CCAC surface.[57,58]

The surface morphology, elemental distribution, and compositional properties of the synthesised CCAC/Co-ZnO composite were investigated using field emission scanning electron microscopy (FE-SEM) coupled with energy-dispersive X-ray spectroscopy (EDX), as depicted in Fig. 3a. The micrograph demonstrates that Co-doped ZnO nanoparticles, exhibiting irregular morphologies, are uniformly dispersed across the carbon surface and form heterojunctions in close contact with the carbon material. In specific regions, particle agglomeration was observed, probably contribute to improved photocatalytic activity by increasing reactive surface sites and facilitating charge carrier transport.[59] The EDX spectrum of the nanocomposite is displayed in Fig. 3b. The spectrum validates the presence of Zn, O, C, and Co, indicating that cobalt was successfully incorporated into the ZnO lattice and disseminated across the carbon surface. The spectrum shows no evidence of elemental impurities, further confirming the purity of the synthesized composite.

The morphological features and average particle size of the CCAC/Co-doped ZnO nanoparticles were studied *via* transmission electron microscopy (TEM), as illustrated in Fig. 3c. TEM analysis revealed that the produced nanoparticles were partly spherical, with an average diameter of 5.67 ± 2.5 nm. Notably, the particles demonstrated a tendency to agglomerate, a characteristic further substantiated by the SEM result, which reveal aggregated nanoparticle regions throughout the sample surface. The interplanar spacing of the lattice fringes in the HR-TEM image (Fig. 3d) is 0.292 nm, corresponding to the (100) crystal plane of ZnO. Furthermore, the selected area electron diffraction (SAED) pattern as shown in Fig. 3e, revealed

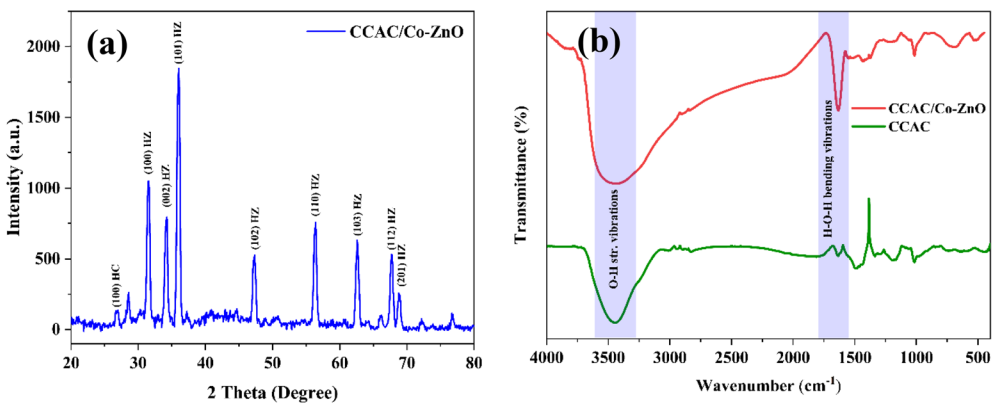

Fig. 2 (a) XRD pattern, and (b) FT-IR spectra of synthesized nanomaterial.

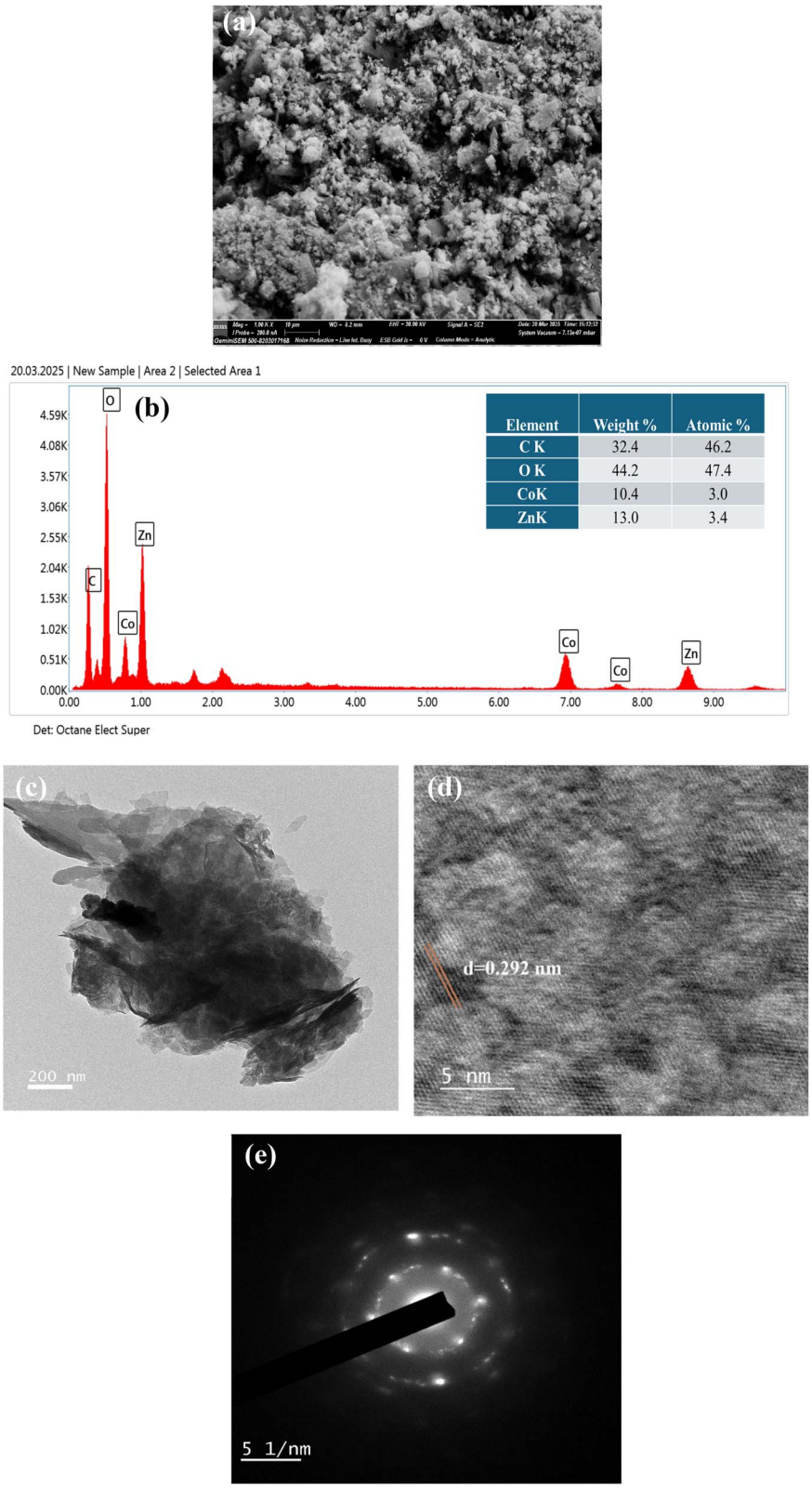

Fig. 3 (a) SEM image, (b) EDX spectrum (c) TEM image, (d) HRTEM image, and (e) SAED image of CCAC/Co-ZnO.

a polycrystalline material characterized by discrete diffraction spots, which may be attributed to the presence of ZnO particles embedded within the CCAC matrix.[60] The concentric rings of various crystallographic planes in the SAED patterns corresponded to the (002), (110), and (201) planes of ZnO, in good agreement with the XRD spectrum.

The optical band gap energy (E_g) of ZnO and CCAC/Co-ZnO nanoparticles are vital for selecting the appropriate light energy to eliminate organic contaminants from aquatic tributaries *via* photocatalysis.[61] UV-Vis diffuse reflectance spectroscopy (DRS) was applied to explore the light-harvesting properties of the synthesized photocatalysts as shown in Fig. 4a. As can be observed from the figure that the absorption edge of CCAC/Co-ZnO is shifted into the visible spectrum in comparison to pure ZnO, signifying improved light-harvesting capacity. The red shift is ascribed to the inclusion of Co^{2+} ions, which introduce new energy levels within the band gap of ZnO and promote charge transfer processes, thereby improving photocatalytic activity.

The E_g values were determined using the Kubelka–Munk function and calculated from Tauc plot, which is represented by the following expression:

$$(\alpha h\nu)^n = \mathrm{A}\ (h\nu - E_g) \quad (2)$$

where α = optical absorption coefficient, $h\nu$ = photon energy, K = the proportionality constant, and n = the type of transition.

The E_g values of the synthesized materials were determined from the Tauc plots $(\alpha h\nu)^2$ *vs.* $h\nu$ (Fig. 4b). The pristine ZnO exhibited an E_g of 3.3 eV, while the Co–ZnO/carbon composite showed a substantial reduction in band gap energy of 2.1 eV. The introduction of Co ions effectively reduces the band gap, resulting in a red shift in light absorption from the ultraviolet to the visible spectrum. The presence of mesoporous carbon not only increases the specific surface area but also improves light absorption efficiency, expedites the generation of active sites and charge carriers. These synergistic effects significantly develop the photocatalytic breakdown of BPA driven by visible light. In addition, the valence band (E_{VB}) and conduction band (E_{CB}) potentials of the ZnO nanoparticles were theoretically determined using the Mulliken electronegativity approach in combination with the calculated band gap energy.[62,63]

A photoluminescence (PL) spectral analysis was performed at an excitation wavelength of 377 nm to obtain a more profound understanding of the behaviour of charge carriers.[64] Generally, a decline in PL intensity suggests a reduced recombination rate of photogenerated electron–hole pairs. The PL spectra (Fig. 4c) exhibit a significant drop in intensity for the CCAC/Co-ZnO composite in comparison to pure ZnO, suggesting a substantial decrease in the recombination rate of photoexcited e^-/h^+ pairs. This implies that the composite structure significantly improves the separation of charge carriers, thereby increasing the availability of reactive species for photocatalytic processes. The construction of a heterojunction between the porous carbon and Co-ZnO is responsible for the improved performance, as it facilitates efficient charge transfer and prevents recombination.[65] This outcome demonstrates that the synthesised nanocomposite possesses enhanced photocatalytic efficiency relative to pure ZnO.

X-ray photoelectron spectroscopy (XPS) investigation was conducted to examine the composition and elemental state of the CCAC/Co-ZnO nanocomposite. The resulting spectra are

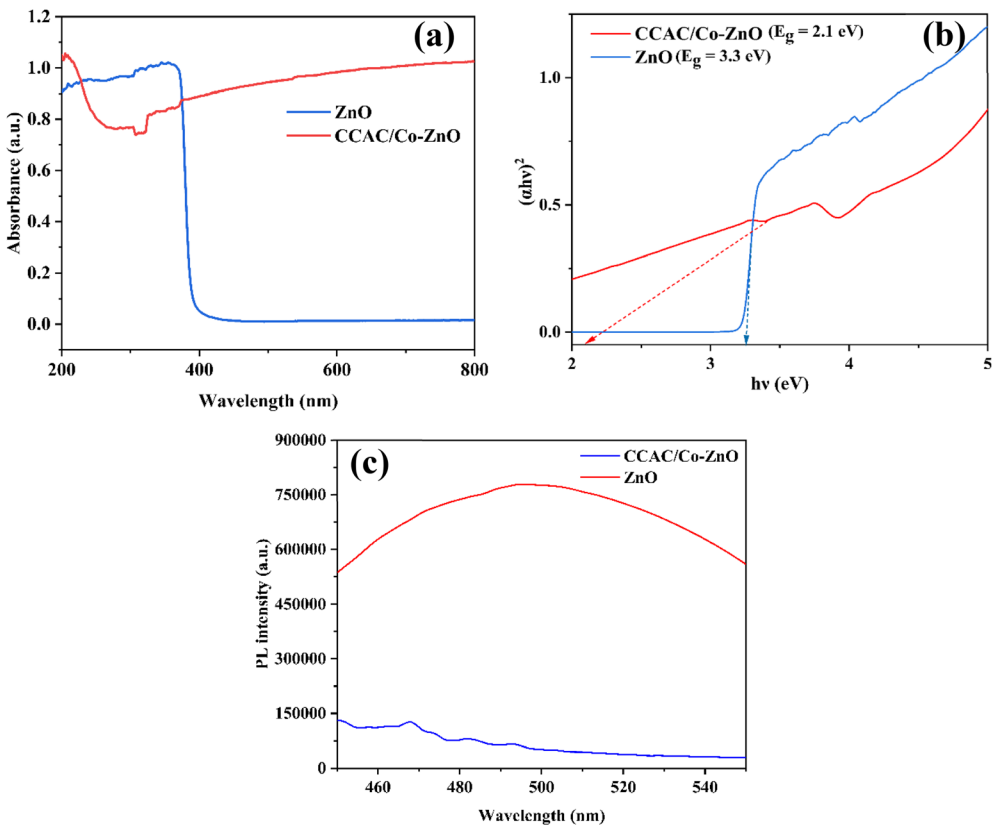

Fig. 4 (a) UV-DRS spectra, (b) Tauc plot, and (c) PL spectra of ZnO and CCAC/Co-ZnO photocatalyst.

shown in Fig. 5a–e. The wide spectrum indicated the coexistence of Zn, Co, O and C elements in the nanoparticles. The deconvoluted C 1s XPS spectrum reveals three distinct peaks at 282.9, 285.2 and 287.7 eV, corresponding to C–C/C–H bonds (graphitic carbon from CCAC), C–O groups (hydroxyl or epoxy), and COO^- species (carboxylate groups), respectively. The peaks corroborate the existence of several oxygen-containing functional groups on the surface of the nanocomposite. The O 1s spectrum showed binding energies at 529.9 eV, 531.4 eV, and 532.9 eV, indicating oxygen vacancies, oxygen atomic orientations, and chemisorbed O_2^- species, respectively in the ZnO lattice. The two peaks observed at binding energies of 797.2 eV and 783 eV, representing Co $2p_{1/2}$ and Co $2p_{3/2}$, respectively, confirming the presence of Co^{2+} ions.[66] The high-resolution XPS spectrum of Zn 2p indicates two distinct peaks: one at 1022.7 eV for Zn $2p_{3/2}$ and another at 1045.8 eV for Zn $2p_{1/2}$, signifying the presence of Zn^{2+} oxidation state in ZnO particles.[67]

The surface area and pore structure of the synthesized photocatalyst were performed using the Brunauer–Emmett–Teller (BET) method. According to the findings, the porous carbon (CCAC) demonstrates a greater specific surface area of 846.29 $m^2\ g^{-1}$,[50] whereas the Co–ZnO/carbon nanocomposite has a reduced surface area of 367.755 $m^2\ g^{-1}$. This reduction is most likely owing to the integration of Co and ZnO nanoparticles, which may partially block the pores of the carbon surface, implying that these particles occupy a large percentage of the porous material. The CCAC/Co-ZnO composite has a total pore volume of 0.085 $cm^3\ g^{-1}$ and an average pore diameter of 3.627 nm, indicating a type IV isotherm, which corresponds to mesoporous materials as classified by IUPAC. The existence of such mesoporosity, along with a relatively large surface area, is expected to improve photocatalytic efficiency by increasing active sites and aiding reactant diffusion.

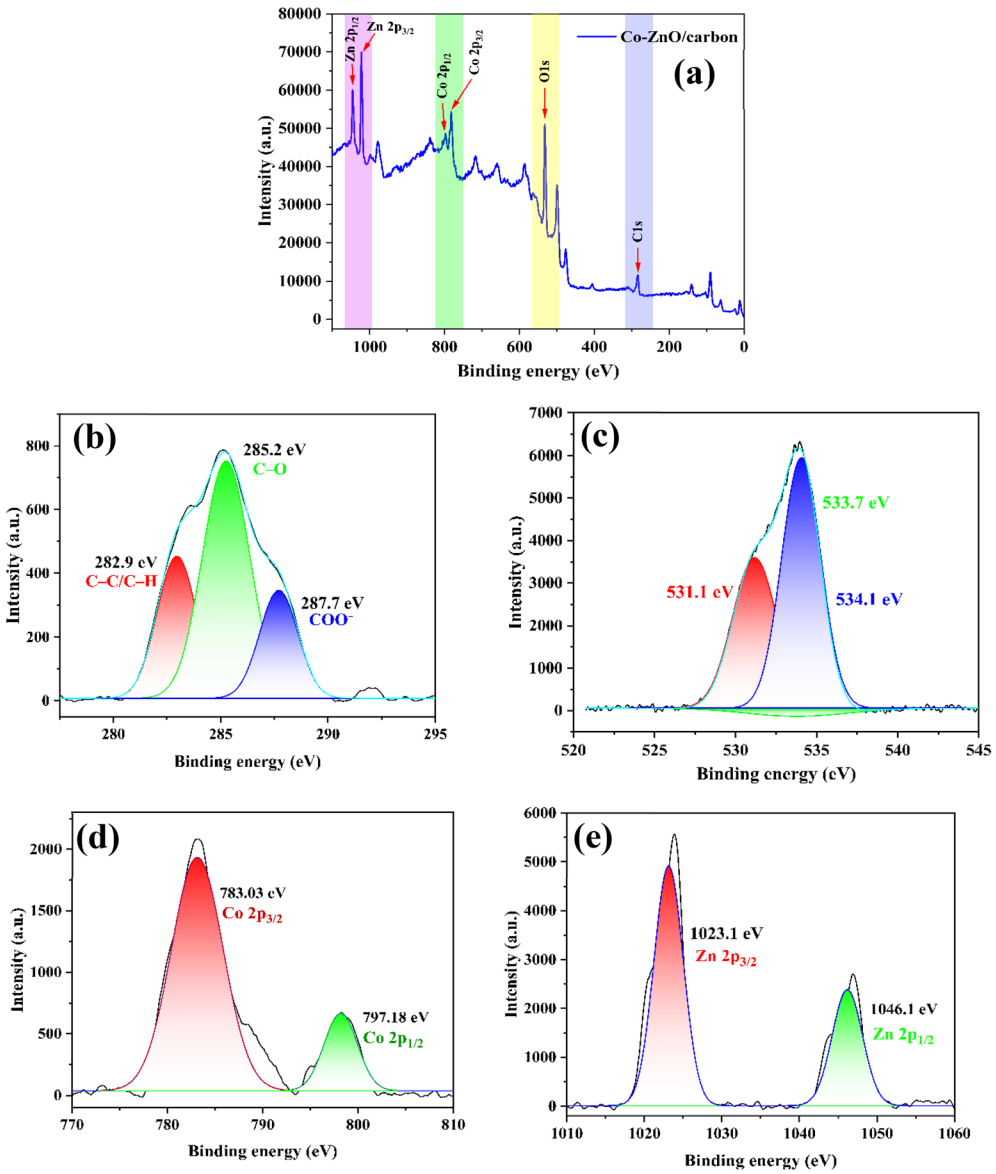

Fig. 5 XPS spectra of CCAC/Co-ZnO nanocomposite: (a) survey scan, (b) C 1s (c) O 1s, (d) Co 2p, and (e) Zn 2p.

3.2. Photocatalytic degradation of BPA

The photocatalytic activity of pure ZnO, Co-ZnO and CCAC/Co-ZnO under visible light was evaluated using BPA (20 mg L^{-1}) as the target pollutant. Fig. 6 illustrates that the degradation efficiency of BPA increased with irradiation time, which is due to improved charge separation on the catalyst surface.[68] The CCAC/Co-ZnO photocatalyst showed the best photocatalytic performance, removing 99.67% of BPA after 60 min. In comparison, the Co-ZnO composite exhibited a degrading efficiency of 60%, but pristine ZnO attained just 34% under identical conditions.

To further elucidate the individual contributions of adsorption and photocatalysis to BPA removal, control experiments were conducted using pure CCAC and a photocatalytic blank (without catalyst) under identical experimental conditions. The blank experiment showed negligible BPA degradation, indicating that direct photolysis under visible light was insignificant. In contrast, pure CCAC exhibited moderate BPA removal due to its adsorption capacity, which can be attributed to the porous structure and abundant surface functional groups of the AC (Fig. S3). However, the removal efficiency obtained with CCAC alone was significantly lower than that of the CCAC/Co-ZnO nanocomposite, confirming that adsorption alone cannot account for the high BPA degradation efficiency observed.

The enhanced photocatalytic performance of the CCAC/Co-ZnO nanocomposite can be attributed to the effective suppression of charge carrier recombination and improved visible-light absorption, which facilitates efficient adsorption and photocatalytic degradation of BPA.[69]

3.3. Influence of reaction conditions

To prevent using photocatalysts excessively in photocatalytic experiments, the required amount of catalyst needs to be adjusted. The effect of CCAC/Co-ZnO dosage on the photocatalytic degradation of BPA under visible light exposure was performed by varying the catalyst concentration from 0.05 g L^{-1} to 0.25 g L^{-1} as shown in Fig. 7a. At an optimal catalyst loading of 0.1 g L^{-1}, the degradation efficacy of BPA was observed to increase as the catalyst dosage was increased, resulting in a maximum of 99.7% degradation within 60 min. This implies that the used catalyst was effectively activated by visible light irradiation, resulting in the indirect formation of reactive species and the increased generation of photoinduced electron–hole (e^-/h^+) pairs. However, increasing the catalyst amount beyond 0.1 g L^{-1} range resulted in a decrease in degradation performance. The decrease in removal effectiveness seen with increasing catalyst dosages could be explained by the fact that the photocatalyst is not effectively activated due to the increased light dispersion as well as reduced light penetration.[70] Additionally, an increase in catalyst dosage leads to an increase in particle–particle interactions (agglomeration), which subsequently diminishes the effective surface area available for pollutant adsorption and light absorption. As a result, the photodegradation rate drops as the catalyst concentration rises. Similar observations have been reported in previous studies.[71,72]

The effect of initial BPA concentration on photocatalytic degradation was investigated by increasing BPA levels from 10 to 50 ppm while holding other parameters constant (solution pH at 6, catalyst amount at 0.1 g L^{-1}). As shown in Fig. 7b, increasing the initial BPA concentration led to a decrease in degradation efficiency from 98% to 72.4%. This reduction could be ascribed to the increased amount of pollutant molecules adsorbed onto the catalyst surface at high concentrations, resulting in surface saturation. As a result, photon penetration is limited, preventing effective light–catalyst interaction. These factors combine to reduce the generation of excitons and hydroxyl radicals, resulting in a decrease in photocatalytic activity at higher concentrations. Prior studies have revealed comparable findings found that increasing the initial concentration of BPA considerably lowers its degradation efficiency, corroborating the observed pattern.[73]

The pH significantly influences photocatalytic processes by affecting the surface charge characteristics of the semiconductor material. To evaluate the effect of pH on BPA degradation, experiments were conducted by varying the solution pH from 2 to 12, while maintaining a constant catalyst dosage of 0.1 g L^{-1} and an initial BPA concentration of 20 ppm. The pH of the reaction mixture was adjusted using 0.1 M NaOH and HCl solutions. As shown in Fig. 7c, the photodegradation efficiency of BPA increases with increasing pH from 2.0 to 6.0, however decreases under alkaline circumstances after 60 min of visible light exposure. The pH range between the composite's point of zero charge (6.7) (Fig. 7d) and the pK_a of BPA (9.6) is crucial in determining photocatalytic behaviour, as it significantly affects the catalyst's surface charge and the ionic state of the pollutant, thereby influencing adsorption and degradation efficiency. Under weak acidic conditions (pH < 6.7), the catalyst surface becomes positively charged, enhancing the adsorption of negatively charged BPA species and potentially increasing photocatalytic efficiency. Conversely, at pH levels exceeding 10, both the catalyst surface and the BPA molecules are negatively charged, which may cause electrostatic repulsion, limiting adsorption and consequently lowering degrading performance. Moreover, pH can influence the generation and stability of ROS, which serve as vital intermediates in the degradation pathway. Optimal pH conditions promote the production of hydroxyl

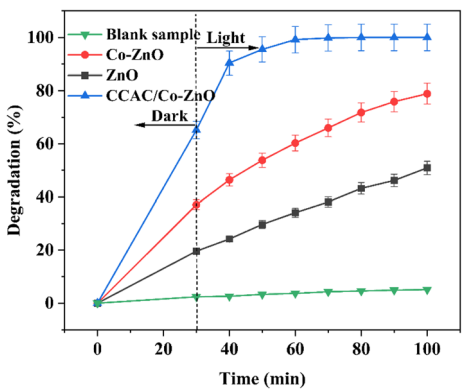

Fig. 6 Degradation of bisphenol A (BPA) using different catalyst.

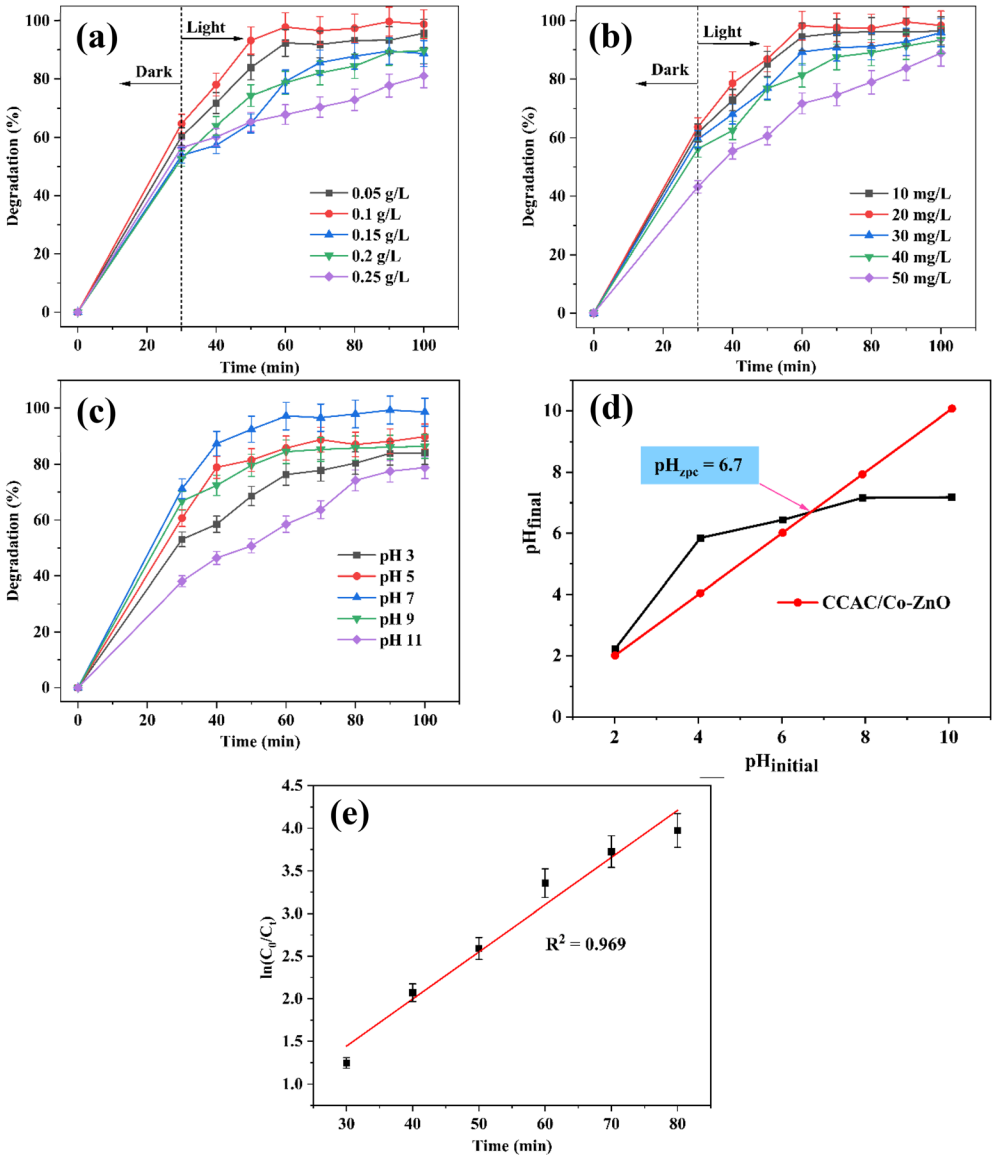

Fig. 7 Effect of (a) catalyst amount, (b) BPA concentration, (c) pH, (d) zero point charge, and (e) kinetic studies.

radicals and other oxidative species, facilitating the breakdown of BPA.[74]

The degradation kinetics of BPA can be explained using a pseudo-first order (PFO) reaction model based on the Langmuir–Hinshelwood (L–H) kinetic framework.[75] This model is mathematically represented as follows:

$$\ln\left(\frac{C_0}{C_t}\right) = k_{ap}t \quad (3)$$

$$t_{1/2} = \frac{\ln 2}{k_{ap}} \quad (4)$$

where C_0 = initial BPA concentration, C_t = concentration at time t, $t_{1/2}$ = the half-life period, and k_{ap} is the apparent reaction rate constant, respectively.

Fig. 7e presents the graph of $\ln(C_0/C_t)$ against reaction time, indicating the kinetic characteristics of BPA photodegradation. The experimental findings provide a strong linear correlation (R^2 > 0.969), validating that the reaction adheres to PFO kinetics. The slope of the fitted line yielded an apparent rate constant (k_{ap}) of 0.055 min^{-1}, which corresponds to a half-life ($t_{1/2}$) of 12.6 min. These kinetic parameters demonstrate that the synthesised catalyst promotes a reasonably fast degradation rate under visible-light irradiation.

3.4. Recyclability and photostability of nanocomposite

The reusability of a photocatalyst is a vital consideration for its sustained implementation in large-scale processes. To evaluate the reusability of the CCAC/Co-ZnO photocatalyst, its degradation efficacy for BPA was tested across five successive cycles (Fig. 8a). The synthesized catalyst demonstrated excellent performance, attaining 97.4% degradation of BPA during the initial cycle. Subsequently, the catalytic efficiency exhibited

a gradual decrease, attaining 84.38% by the fourth cycle. Although the reduction is slight, it highlights the necessity for further research to elucidate the underlying mechanisms responsible for the loss of activity. The slight decline in photocatalytic efficiency observed over successive cycles may be attributed to various factors: (a) accumulation of BPA degradation intermediates on the catalyst surface and the agglomeration of nanoparticles, and (b) the continual loss of nanocomposite material during the recovery and reuse procedures.[76] These factors collectively impede visible-light irradiation and diminish the quantity of active sites available for photocatalysis. Notably, after multiple cycles, the nanocomposite exhibited a degradation efficiency of around 77.63% in the fifth cycle, underscoring its sustained catalytic activity.

Furthermore, the photostability of the CCAC/Co-ZnO nanocomposite was assessed using XRD analysis of the material collected after five reuse cycles. The resulting spectrum was compared to that of the unmodified nanocomposite (Fig. 8b). The examination of XRD peaks prior to and following BPA degradation indicated no significant changes in the characteristic XRD peaks. This finding indicates that the CCAC/Co-ZnO nanocomposite preserves its structural integrity throughout the photocatalytic process, demonstrating stable and reusable photocatalyst. The lack of substantial structural alterations suggests that the nanocomposite maintains its effectiveness and stability after numerous breakdown processes.

3.5. Real wastewater applications

To evaluate the practical applicability of the catalyst (CCAC/Co-ZnO)) in real water systems, two representative water matrices, including DDW and real wastewater source, were employed for the degradation experiments. Wastewater samples were collected from Mokokchung district, Nagaland, India and stored in glass containers. Since the native concentration of BPA was undetectable, the samples were spiked with 20 ppm of BPA to conduct degradation experiments. The sampling location and water quality analysis procedures are provided in Fig. S4 and Table S2, respectively. The physicochemical characteristics of the wastewater included a pH of 6.52, total dissolved solids (TDS) of 19 ppm, electrical conductivity (EC) of 39 μS cm^{-1}, total hardness (TH) of 84 ppm, and biological oxygen demand (BOD) of 3.3 ppm. Inorganic analysis indicated the presence of sulfate (SO_4^{2-}, 20 ppm), phosphate (PO_4^{3-}, 0.2 ppm), calcium (Ca^{2+}, 4 ppm), magnesium (Mg^{2+}, 48.79 ppm), chloride (Cl^-, 4.26 ppm), and alkalinity of 4 ppm.

Photocatalytic experiments performed under optimized conditions (catalyst dose: 0.1 g L^{-1}, pH: 7.0, reaction time: 60 min) demonstrated that the CCAC/Co-ZnO nanocomposite exhibited significant photocatalytic activity, achieving 86.42% degradation of BPA in real wastewater, compared to 99.67% in DDW (Fig. 9). The comparatively lower efficiency observed in real wastewater can be attributed to the complex water matrix containing coexisting inorganic ions. In particular, the relatively high concentration of Mg^{2+} may promote catalyst aggregation and surface passivation, thereby reducing the number of available active sites. Additionally, the presence of SO_4^{2-} and Cl^- ions may act as scavengers of hydroxyl radicals ($^{\bullet}OH$), which can hinder the oxidative degradation process.

3.6. Role of scavengers

To understand the mechanism of BPA photodegradation, it is imperative to explore the role of ROS and identify the specific reactive radicals involved in the process. The reactive species responsible for BPA degradation were identified through a series of diagnostic analyses using the Co-ZnO/carbon

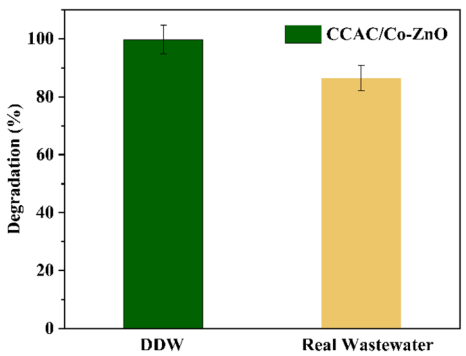

Fig. 9 Degradation of BPA in the real wastewater environment.

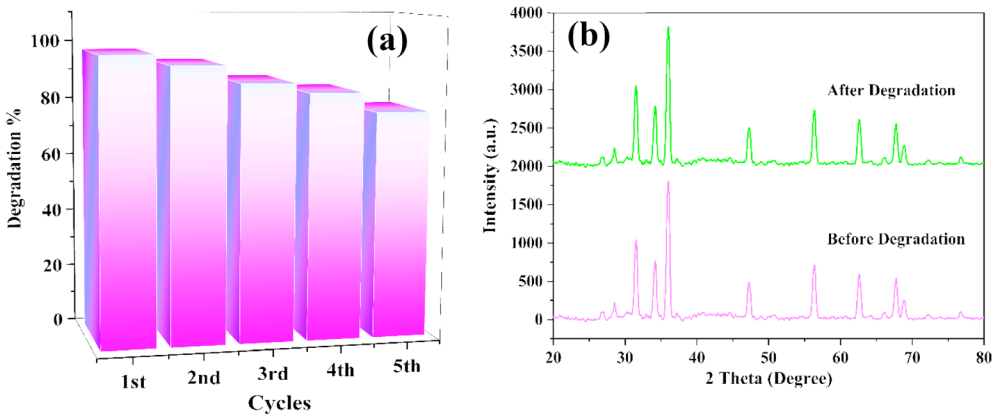

Fig. 8 (a) Degradation % of nanocomposite up to five cycles, and (b) XRD spectra of nanocomposite (before and after degradation).

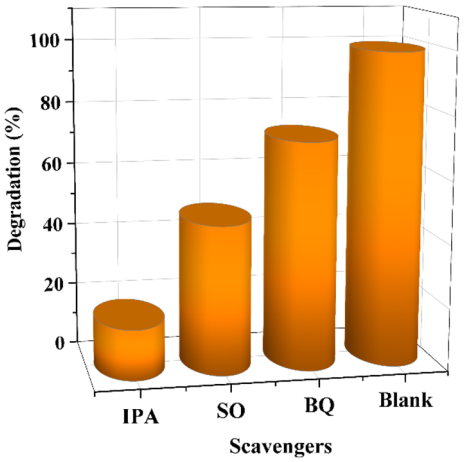

Fig. 10 Effect of different radical scavengers for BPA degradation.

composite. The experiments were conducted in the presence of isopropanol (IPA, $^{\bullet}OH$ scavenger), benzoquinone (BQ, $^{\bullet}O_2^-$ inhibitor) and sodium oxalate (SO, h^+ scavenger) respectively. The degradation efficiency of BPA was substantially reduced by the addition of these scavengers compared to the blank photocatalyst. The photodegradation efficiency of BPA declined from 99.7% to 72%, 47%, and 16% upon the addition of BQ, SO and IPA respectively (Fig. 10). Scavengers were effective in the following order: IPA > SO > BQ. This investigation found that all major reactive species, including hydroxyl radicals ($^{\bullet}OH$), photogenerated holes (h^+) and superoxide radicals ($^{\bullet}O_2^-$) contributed to the photocatalytic destruction of BPA.

3.7. Mineralization

Total organic carbon analysis was conducted at different concentrations (20–50 mg L^{-1}) to ascertain the complete mineralization of BPA using a photocatalyst, while maintaining other parameters constant. Fig. 11 illustrates that 81.02% of the BPA achieved effective mineralization following a 60 min reaction period for 20 mg L^{-1} concentration. The reduction in TOC signifies the oxidation and destruction of the organic contaminant into less harmful substances. Nevertheless, the mineralization efficiency diminished to 54.4% upon elevating the initial BPA concentration to 50 mg L^{-1}, suggesting that increased contaminant levels may impede the process, possibly as a result of inadequate ROS.[77] The above observation is supported by the LC-MS approach, as explained in the following sections.

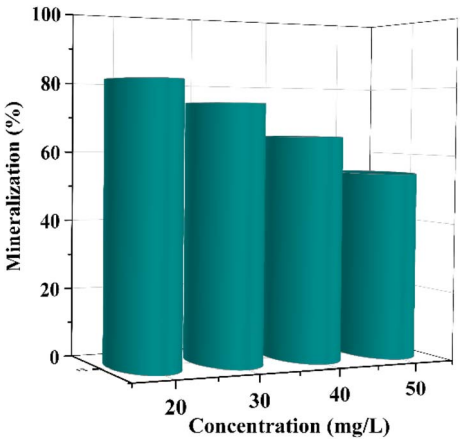

Fig. 11 Mineralization (%) of BPA at various concentration.

3.8. LC-MS analysis

LC-MS analysis was conducted to investigate the intermediate compounds produced during the photocatalytic breakdown of BPA. Fig. S5 and Table S3 outline the spectrum fragmentation peaks, and the corresponding intermediates of BPA identified after 60 min of visible light exposure. A comprehensive photocatalytic degradation pathway was proposed based on these insights, as illustrated in Scheme 1. Initially, the hydroxyl radical ($^{\bullet}OH$) attacked the C–H bond of the benzene ring, forming a hydroxylated intermediate, P1 ($m/z = 243$). Previous research using density functional theory (DFT) has shown that the carbon atoms closest to the benzene ring's hydroxyl group are the most susceptible to radical and electrophilic attacks.[78] The hydroxylation process would therefore be preferentially initiated, which is in accordance with the results that have been identified. Subsequently, the degradation proceeded along two possible reaction pathways. For pathway I, further hydroxylation produced intermediate P2 ($m/z = 241$) from P1. For pathway II, P1 was responsive to phenyl ring cleavage, resulting in fragment products with a single benzene ring, including P3 ($m/z = 167$), P4 ($m/z = 135$), P5 ($m/z = 133$), P6 ($m/z = 110$) and P7 ($m/z = 94$). Researchers have identified intermediates with similar structures in the degradation of serial bisphenols.[79,80] These intermediates may reach relatively high abundance and the main degrading mechanism identified was due to loss of benzene fragments.[81] Under continuous oxidation, the ring structure would be entirely opened, leading to the formation of smaller molecular products such as P8 ($m/z = 90$), P9 ($m/z = 112$), P10 ($m/z = 60$), and P11 ($m/z = 106$). Finally, they could breakdown into CO_2 and H_2O, resulting in mineralisation of BPA.

3.9. Proposed degradation mechanism of BPA pollutant

The probable degradation mechanism of BPA under simulated visible light irradiation on the CCAC/Co-ZnO photocatalyst is illustrated in Fig. 12. Consequently, when the energy of the irradiation light exceeds the band gap energy of ZnO, the excited electrons (e^-) from the VB of ZnO are transferred to its CB, concurrently generating an equivalent number of holes (h^+) in the VB. Besides, the incorporation of Co-ions into the ZnO framework introduces new energy levels between the CB and VB of ZnO, serving as charge-trapping centres that impede the recombination rate of electron–hole pairs and extend the lifetime of photogenerated carriers. Consequently, given that porous carbon serves as an appropriate electron acceptor and transfer medium, the excited electrons can rapidly migrate from the conduction band of ZnO to the CCAC, thereby inhibiting charge recombination. The following reactions represent the electron transfer process:

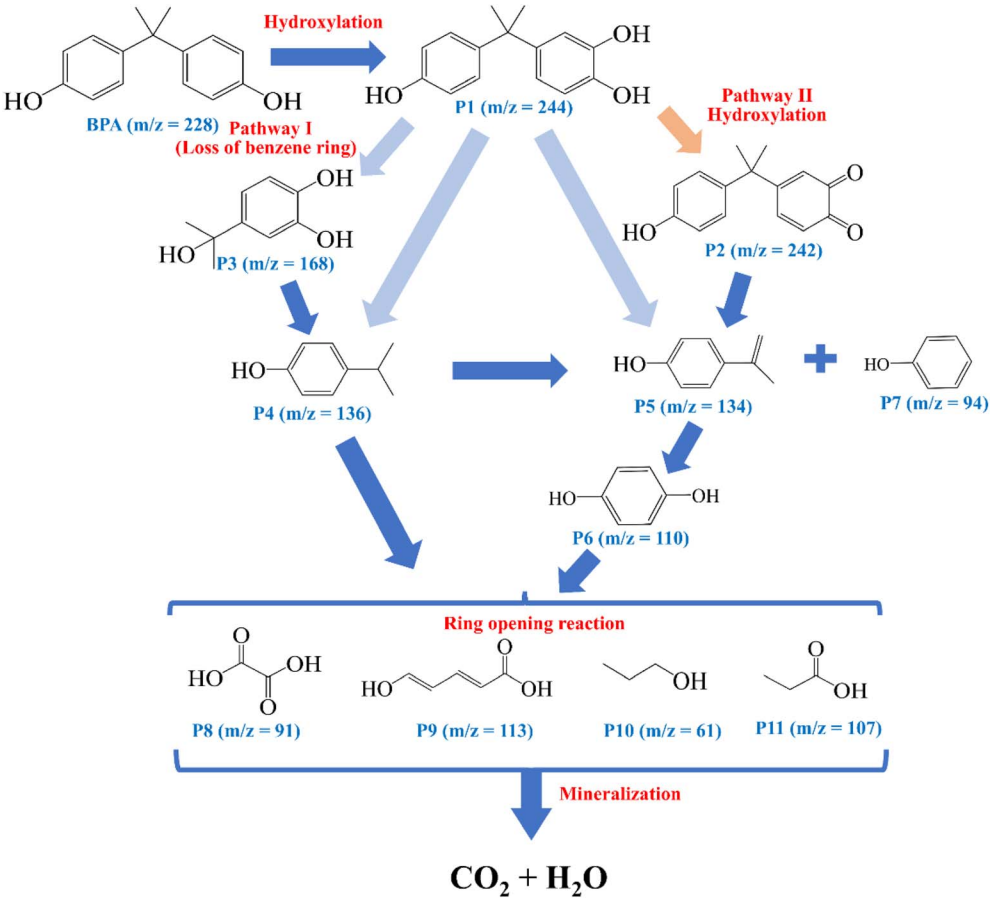

Scheme 1 Possible degradation pathways of BPA using CCAC/Co-ZnO photocatalyst.

$$\text{Co-ZnO/CCAC} \xrightarrow{h\nu} \text{Co-ZnO}(e^- + h^+)/\text{CCAC} \quad (5)$$

$$\text{Co-ZnO}(e^- + h^+)/\text{CCAC} \rightarrow \text{Co-ZnO}(h^+)/\text{CCAC}(e^-) \quad (6)$$

Subsequently, the photoexcited electrons interact with oxygen molecules, resulting in the formation of reductive superoxide radicals ($^{\bullet}O_2^-$). On the other hand, oxidative hydroxyl radicals ($^{\bullet}OH$) can be produced when holes react with water molecules (H_2O) or hydroxyl ions (OH^-). ROS, specifically superoxide and hydroxyl radicals, engage in the photodegradation of BPA molecules, facilitating their decomposition into CO_2, H_2O, and various mineralization products, as seen in the reactions below:

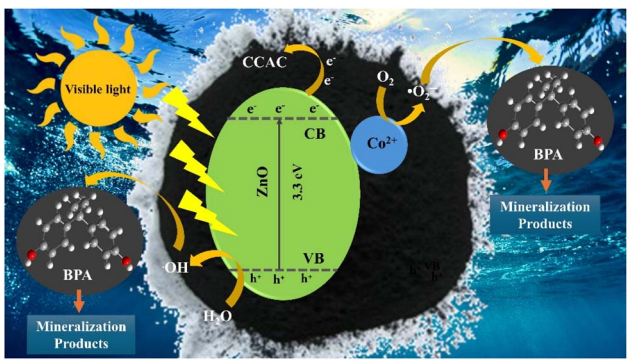

Fig. 12 Illustration of the plausible BPA photocatalytic degradation mechanism over CCAC/Co-ZnO nanocomposite.

$$\text{CCAC}\ (e^-) + O_2 \rightarrow \text{CCAC} + {}^{\bullet}O_2^- \quad (7)$$

$$\text{Co-ZnO}(e^-) + O_2 \rightarrow \text{Co-ZnO} + {}^{\bullet}O_2^- \quad (8)$$

$$2({}^{\bullet}O_2^-) + 2H_2O \rightarrow H_2O_2 + 2OH^- + O_2 \quad (9)$$

$$H_2O_2 + 2({}^{\bullet}O_2^-) \rightarrow {}^{\bullet}OH + OH^- + O_2 \quad (10)$$

$$\text{Co-ZnO}(h^+) + H_2O \text{ or } OH^- \rightarrow \text{Co-ZnO} + {}^{\bullet}OH \quad (11)$$

$$h^+ + OH^- \rightarrow {}^{\bullet}OH \quad (12)$$

$$h^+ + H_2O \rightarrow H^+ + {}^{\bullet}OH \quad (13)$$

$${}^{\bullet}OH/\ {}^{\bullet}O_2^-/h^+\ (\text{ROS}) + \text{BPA} \rightarrow \text{intermediate products} \rightarrow CO_2 + H_2O \quad (14)$$

3.10. Theoretical insights of BPA toxicity and its intermediates

The toxicity of BPA and its degradation intermediates was studied with two toxicity evaluation servers Protox-3 and

ADMETlab 2.0.[82,83] Herein, the median lethal concentration for *Fathead minnow* (LC_{50}-96 h), median lethal concentration for *Daphnia magna* (LC_{50}-48 h), bioaccumulation factors, LD_{50}, IGC_{50} and mutagenicity were chosen as main toxicity indicators.[84,85] BPA and its degradation intermediates (P1 to P11) have LD_{50} values greater than 100, which can be classified as harmless, while P9 with the highest LD_{50} value making it even less toxic relatively than BPA. As shown in Fig. S6a, only the LC_{50}-96 h of P1 and P2 were slightly higher than that of BPA while P3, P4, P5, P6, P7 and P9 with lower LC_{50}-96 h were be classified as not harmful substance. Also, P8, P10 and P11 with the least LC_{50}-96 values can be considered slightly toxic. Similar results were obtained from LC_{50}-48 h where P1 and P2 exhibited higher values than BPA (Fig. S6a) itself and P3, P4, P5, P6, P7, P9 and P11 with lower LC_{50}-48 h can be classified as not harmful substance. P8 and P10 with lower LC_{50}-48 h can be considered as slightly toxic. Compared with BPA, the bioaccumulation factor of the degradation intermediates was reduced considerably (Fig. S6b). BPA and its degradation intermediates (P1 to P11) have LD_{50} values greater than 100, which can be classified as harmless, while P9 with the highest LD_{50} value making it even less toxic relatively than BPA (Fig. S6c).

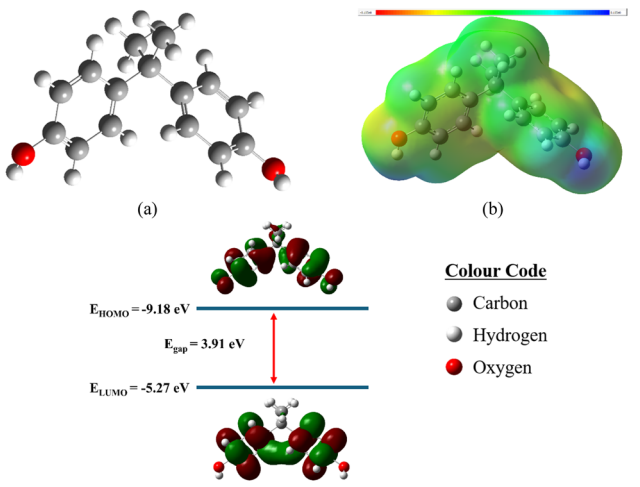

Fig. 13 (a) Optimized structure, (b) E_{gap} and (c) ESP surfaces showing charge distribution of BPA.

Similarly, for IGC_{50}, BPA was found to be moderately toxic with P1 and P2 having a higher IGC_{50} value supporting its relatively lower ecological impact in terms of growth inhibition. However, P3 to P7 demonstrated greater environmental toxicity than BPA with lower IGC_{50} values than P1 and P2. The most environmentally toxic degradation products, based on IGC_{50} were P10, P11 and P8 indicating that these compounds could exert strong growth-inhibitory effects on aquatic organisms even at relatively low concentrations (Fig. S6b).

In addition, BPA has a high mutagenicity which can be classified as toxic. However, the mutagenicity of degradation products except P7 was significantly reduced (Fig. S6d).

The above analysis indicates that the toxic BPA molecules were successfully degraded during the reaction process and converted into less harmful intermediate species. Similar observations have also been reported in various studies.[86,87] Further verification of the environmental friendliness of the developed treatment process by performing acute toxicity test for the reaction solution containing BPA and its degradation products warrants future investigations.

3.11. Frontier orbital theory analysis of BPA using conceptual DFT in photocatalytic degradation

Conceptual DFT calculations were conducted using Gaussian 16 to investigate the reactivity of BPA during photocatalytic degradation, with visualizations generated using GaussView 6.0 (Fig. 13). The calculations focused on frontier molecular orbitals (FMOs), electrostatic potential (ESP) surfaces, and Fukui reactivity indices to elucidate the electronic properties and identify reactive sites of BPA under photocatalytic conditions.[88] The optimised BPA structure consists of two phenyl rings connected by an isopropylidene bridge in a nearly planar arrangement, with a C–C bond length of ~1.54 Å. The computed HOMO and LUMO energies are −9.18 eV and −5.27 eV, respectively, resulting a HOMO–LUMO energy gap of 3.91 eV, which suggests increased electronic polarizability and favorable charge-transfer capability during photocatalytic reactions.[89] The ESP surface, mapped within a potential range of −0.105 to +0.105 a.u., reveals strongly negative potential regions localized around the phenolic –OH groups, reflecting high electron density associated with oxygen lone pairs, while relatively positive regions are distributed over the aromatic hydrogen

Table 1 Photocatalytic performance comparison of the synthesized nanocomposite with reported photocatalysts for BPA degradation

Targeted pollutant	Photocatalysts	Catalyst dosage	BPA initial concen.	Light intensity	Irradiation time (min)	Performance of photocatalyst (%)	Ref.
BPA	ZnO/rGO	0.025 g L^{-1}	10 mg L^{-1}	—	30	93.1	92
	Ag_2O_x(1 wt%)/ST	0.05 g L^{-1}	10 mg L^{-1}	1000 mW cm^{-2}	180	98	93
	MOF-derived $Bi_{12}O_{17}Cl_2$ Nanoflakes	0.5 g L^{-1}	20 mg L^{-1}	—	60	94.3	94
	Fe/Cu@NC-x	0.2 g L^{-1}	20 mg L^{-1}	—	30	98	95
	ZnO/carbon xerogel	1 g L^{-1}	10 mg L^{-1}	110 W m^{-2}	300	78	96
	ZnO/OCN nanocomposite	0.5 g L^{-1}	10 mg L^{-1}	—	180	92.5	97
	CCAC/Co-ZnO	0.1 g L^{-1}	20 mg L^{-1}	—	60	99.6	Present study

atoms and the alkyl bridge. The charge distribution indicates that the phenolic oxygen atoms serve as primary sites for electrophile attraction, whereas the aromatic rings are more prone to nucleophilic and radical-mediated interactions.[90] Fukui function analysis further corroborates this behavior: the electrophilic fukui function (f^-) designates the phenolic oxygen atoms and adjacent carbon atoms as the most favorable sites for oxidation by photogenerated holes and hydroxyl radicals, whereas the nucleophilic fukui function (f^+) emphasizes the aromatic π-system as a favored region for electron acceptance. The radical fukui function (f^0) substantiates aromatic rings as primary sites for radical assault (Fig. S7).[91] These findings suggest that BPA degradation initiates at electron-rich phenolic and aromatic sites *via* synergistic electron-transfer and ROS driven pathways under photocatalytic conditions.

3.12. Comparison studies

The photocatalytic degradation efficiency of BPA attained by the CCAC/Co-ZnO nanocomposite was compared with several nanocomposite systems reported in the literature, as outlined in Table 1. The findings demonstrate that the synthesized photocatalyst exhibit significantly improved BPA degradation efficiency relative to previously studied materials. The synthesized nanocomposite exhibits significant potential as an effective photocatalyst for the removal of BPA from wastewater.

4. Conclusion

In this work, a novel photocatalyst based on *Croton caudatus*-derived activated carbon decorated with Co-doped ZnO nanoparticles is developed, which has not been previously investigated. The synergistic incorporation of these components improves charge separation *via* reduce band gap of 2.1 eV, photostability, and degradation efficiency relative to conventional single- or binary-component photocatalysts for BPA removal. Under ideal conditions, the photocatalyst showed great efficacy, attaining 99.67% BPA degradation and 81% mineralization after 60 min of visible light illumination. The L-H model showed that the degradation process followed PFO behavior, with a $t_{1/2}$ of 12.6 min and an apparent rate constant (k_{ap}) of 0.055 min^{-1}, respectively. Scavenger tests revealed that hydroxyl radicals played the significant role for the breakdown process, followed by photogenerated holes and superoxide radicals. Reusability tests showed that the catalyst maintained 77.63% efficiency after five consecutive cycles without significant loss of its activity, confirming its good stability and reusability. LC-MS investigation of BPA degradation showed a possible pathway leading to complete mineralization of carbon dioxide and water. DFT calculations further elucidated the mechanisms underlying the enhanced generation of ROS, providing valuable insights into the photocatalytic degradation pathways. Overall, the findings of this work demonstrate the potential of cost-effective and facilely synthesized photocatalyst as promising materials for addressing organic contamination in wastewater treatment applications.

Conflicts of interest

There are no conflicts to declare.

Data availability

The data supporting this article have been included as part of the supplementary information (SI). Additional information may be obtained from the corresponding author upon reasonable request. Supplementary information is available. See DOI: https://doi.org/10.1039/d6ra00641h.

References

1 E. Baralla, V. Pasciu, M. V. Varoni, M. Nieddu, R. Demuro and M. P. Demontis, *Sci. Total Environ.*, 2021, **785**, 147263.
2 P. Loganathan, S. Vigneswaran, J. Kandasamy, T. V. Nguyen, A. K. Cuprys and H. Ratnaweera, *Chemosphere*, 2023, **328**, 138560.
3 K. Czarny-Krzymińska, B. Krawczyk and D. Szczukocki, *Chemosphere*, 2023, **315**, 137763.
4 M. H. Mahmoudian, A. Mesdaghinia, A. H. Mahvi, S. Nasseri, R. Nabizadeh and M. H. Dehghani, *J. Environ. Health Sci. Eng.*, 2022, **20**, 617–628.
5 C. Naveira, N. Rodrigues, F. S. Santos, L. N. Santos and R. A. Neves, *Environ. Pollut.*, 2021, **268**, 115911.
6 H. J. Lehmler, B. Liu, M. Gadogbe and W. Bao, *ACS Omega*, 2018, **3**, 6523–6532.
7 J. Chudzińska, B. Woźniak, M. Sprynskyy, I. Nowak and A. Feliczak-Guzik, *Int. J. Mol. Sci.*, 2023, **24**, 2878.
8 Y. S. Jung, S. T. Ro, S. W. Kang, H. Lee, J. S. Lee and Y. K. Chae, *J. Clin. Pediatr. Dent*, 2023, **47**, 89–95.
9 J. Liu, K. Sun, R. Zhu, X. Wang, M. G. Waigi and S. Li, *Environ. Pollut.*, 2023, **321**, 121155.
10 C. Oussalah, F. Kaouah, S. Boumaza and M. Trari, *Biomass Convers. Biorefin.*, 2023, **13**, 1–17.
11 Z. Song, Y. Zhang, X. Zhang, X. Zhou, Y. Chen, X. Duan and N. Ren, *Water Res.*, 2023, **237**, 120274.
12 D. Roy, S. Neogi and S. De, *Chem. Eng. J.*, 2022, **428**, 131028.
13 H. T. Nguyen, J. Lee, E. Kwon, G. Lisak, B. X. Thanh, F. Ghanbari and K. Y. A. Lin, *Chemosphere*, 2021, **279**, 130569.
14 T. T. Cao, D. D. Zhou, X. D. Wang and C. Cui, *J. Mol. Liq.*, 2022, **362**, 119622.
15 U.S. Environmental Protection Agency, *Contaminant Candidate List (CCL 5)*, USEPA, Washington, DC, 2023.
16 N. I. Pratiwi, A. Mukimin, N. Zen and I. Septarina, *Sep. Purif. Technol.*, 2021, **279**, 119690.
17 Y. Zhang, Z. Chen, P. Wu, Y. Duan, L. Zhou, Y. Lai, F. Wang and S. Li, *J. Hazard. Mater.*, 2020, **393**, 120448.
18 L. C. Ferreira, J. R. Fernandes, J. A. Peres, P. B. Tavares and M. S. Lucas, *Environ. Res.*, 2021, **200**, 111430.
19 S. Dadvar, B. Shahmoradi, S. Habibi, K. Wantala, T. Suwannaruang, A. Maleki, H. P. Shivaraju and S. M. Lee, *Desalin. Water Treat.*, 2022, **252**, 339–347.

20 A. Farhan, J. Arshad, E. U. Rashid, H. Ahmad, S. Nawaz, J. Munawar, J. Zdarta, T. Jesionowski and M. Bilal, *Chemosphere*, 2023, **310**, 136835.
21 Y. Quan, M. Liu, H. Wu, X. Tian, L. Dou, Z. Wang and C. Ren, *Appl. Surf. Sci.*, 2024, **642**, 158601.
22 H. Ren, F. Qi, A. Labidi, J. Zhao, H. Wang, Y. Xin, J. Luo and C. Wang, *Appl. Catal. B*, 2023, **330**, 122587.
23 K. Davididou, R. Nelson, J. M. Monteagudo, A. Durán, A. J. Expósito and E. Chatzisymeon, *J. Clean. Prod.*, 2018, **203**, 13–21.
24 O. Bechambi, S. Sayadi and W. Najjar, *J. Ind. Eng. Chem.*, 2015, **32**, 201–210.
25 B. Gao, T. M. Lim, D. P. Subagio and T. T. Lim, *Appl. Catal., A*, 2010, **375**, 107–115.
26 M. R. Rajeshwari, M. K. Okla, S. Kokilavani, M. A. Abdel-Maksoud, I. A. Saleh, H. A. Abu-Harirah, T. N. AlRamadneh and S. S. Khan, *Chemosphere*, 2023, **339**, 139529.
27 R. Katwal, H. Kaur, G. Sharma, M. Naushad and D. Pathania, *J. Ind. Eng. Chem.*, 2015, **31**, 173–184.
28 K. Mun, C. Wei, K. Sing and J. Ching, *Water Res.*, 2016, **88**, 428–448.
29 X. Zhou, Y. Mu, S. Zhang, L. Gao, H. Chen, J. Mu, X. Zhang, M. Zhang and W. Liu, *Mater. Res. Bull.*, 2019, **111**, 118–125.
30 M. Ikram, H. Shahid, J. Haider, A. Haider, S. Naz, A. Ul-Hamid, I. Shahzadi, M. Naz, W. Nabgan and S. Ali, *ACS Omega*, 2022, **7**, 39347–39361.
31 M. Li, P. Li, L. Zhang, M. Chen, J. Tang, C. Qin, S. L. J. Lee and S. Lin, *Chem. Eng. J.*, 2022, **434**, 134772.
32 C. Zhu, G. Fang, D. D. Dionysiou, C. Liu, J. Gao, W. Qin and D. Zhou, *J. Hazard. Mater.*, 2016, **316**, 232–241.
33 H. Liang, Y. Zhang, S. Huang and I. Hussain, *Chem. Eng. J.*, 2013, **218**, 384–391.
34 O. Ola and M. M. Maroto-Valer, *J. Photochem. Photobiol.*, 2015, **24**, 16–42.
35 Y. Lu, Y. Lin, D. Wang, L. Wang, T. Xie and T. Jiang, *Nano Res.*, 2011, **4**, 1144–1152.
36 R. Ullah and J. Dutta, *J. Hazard. Mater.*, 2008, **156**, 194–200.
37 J. Zhao, L. Wang, X. Yan, Y. Yang, Y. Lei, J. Zhou, Y. Huang, Y. Gu and Y. Zhang, *Mater. Res. Bull.*, 2011, **46**, 1207–1210.
38 P. Petkova and K. Boubaker, *J. Alloys Compd.*, 2013, **546**, 176–179.
39 S. Kuriakose, B. Satpati and S. Mohapatra, *Adv. Mater. Lett.*, 2015, **6**, 217–223.
40 L. H. Mohammed, F. Gulbagca, R. N. E. Tiri, A. Aygun, M. Bekmezci and F. Sen, *Chem. Eng. J. Adv.*, 2023, **14**, 100495.
41 S. Mustapha, M. M. Ndamitso, A. S. Abdulkareem, J. O. Tijani, D. T. Shuaib, A. O. Ajala and A. K. Mohammed, *Appl. Water Sci.*, 2020, **10**, 1–36.
42 S. L. Ezung, M. Baruah, S. Sharma, R. S. Umdor, I. T. Longchar, B. Giridharan, U. B. Sinha and D. Sinha, *J. Mol. Struct.*, 2025, **1319**, 139434.
43 P. Lisowski, J. C. Colmenares, O. Mašek, D. Łomot, O. Chernyayeva and D. Lisovytskiy, *J. Anal. Appl. Pyrolysis*, 2018, **131**, 35–41.
44 Q. Yao, H. Wang, C. Wang, C. Jin and Q. Sun, *ACS Sustain. Chem. Eng.*, 2018, **6**, 4695–4704.
45 B. T. Son, N. V. Long and N. T. N. Hang, *RSC Adv.*, 2021, **11**, 30574–30596.
46 D. Mohanta, *J. Environ. Chem. Eng.*, 2018, **6**, 356–366.
47 W. Zhou, P. Zhang and W. Liu, *Int. J. Photoenergy*, 2012, **2012**, 28–30.
48 M. Faisal, M. Alsaiari, M. A. Rashed and F. A. Harraz, *J. Taiwan Inst. Chem. Eng.*, 2021, **120**, 313–324.
49 P. Shanmugam, B. Parasuraman, S. Boonyuen, P. Thangavelu, M. S. AlSalhi, A. L. T. Zheng and A. Viji, *Environ. Geochem. Health*, 2024, **46**, 92.
50 S. Sharma, S. L. Ezung, A. Supong, M. Baruah, S. Kumar, R. S. Umdor and D. Sinha, *Chem. Eng. Res. Des.*, 2023, **190**, 777–792.
51 S. Lam, J. Sin, H. Zeng, H. Lin, H. Li, Y. Chai, M. Choong and A. R. Mohamed, *Mater. Sci. Semicond. Process.*, 2021, **123**, 105574.
52 A. Najafidoust, E. A. Asl, H. K. Hakki, M. Sarani, H. Bananifard, M. Sillanpaa and M. Etemadi, *Sol. Energy*, 2021, **225**, 344–356.
53 H. R. Mardani, M. Forouzani, M. Ziari and P. Biparva, *Spectrochim. Acta, Part A Mol. Biomol. Spectrosc.*, 2015, **141**, 27–33.
54 T. Srinivasulu, K. Saritha and K. T. Ramakrishna Reddy, *Mod. Electron. Mater.*, 2017, **3**, 76–85.
55 R. Vinod and M. J. Bushiri, *J. Lumin.*, 2023, **256**, 119628.
56 Z. Lü, Y. Cheng, L. Xue, H. Wang, H. Lin, X. Sun, Z. Miao, S. Zhuo and J. Zhou, *J. Alloys Compd.*, 2022, **898**, 162871.
57 R. Naveenkumar, B. Karthikeyan and S. Senthilvelan, *ChemistrySelect*, 2024, **9**, e202401448.
58 C. K. Bandoh, B. Y. Danu, E. S. Agorku, F. K. Ampong and R. K. Nkum, *Results Mater.*, 2024, **21**, 100515.
59 P. Zhang, T. Wang, X. Chang and J. Gong, *Acc. Chem. Res.*, 2016, **49**, 911–921.
60 S. L. Ezung, M. Baruah, S. Sharma, R. S. Umdor, I. T. Longchar, B. Giridharan, U. B. Sinha and D. Sinha, *J. Mol. Struct.*, 2025, **1319**, 139434.
61 D. A. Kader, A. H. Mohammed, S. J. Mohammed and D. M. Aziz, *RSC Adv.*, 2025, **15**, 18245–18265.
62 M. Mahajan, S. Kumar, J. Gaur, S. Kaushal, J. Dalal, G. Singh, M. Misra and D. S. Ahlawat, *RSC Adv.*, 2025, **15**, 2958–2980.
63 W. B. Soltan, W. Wang, J. Sun, T. Toupance, G. Yu and F. Li, *New J. Chem.*, 2021, **45**, 11051–11067.
64 Q. Ji, H. Yang, J. Li, R. Wang and C. Zhang, *J. Phys. Chem. C*, 2024, **128**, 10520–10527.
65 J. Luo, R. Li, Y. Chen, X. Zhou, X. Ning, L. Zhan, L. Ma, X. Xu, L. Xu and L. Zhang, *Sep. Purif. Technol.*, 2019, **210**, 417–430.
66 E. Kuruvilla, A. S. Nesaraj, V. Jose, D. Padmanabhan and M. Arunkumar, *Mater. Today Commun.*, 2024, **41**, 110227.
67 Y. T. Chung, M. M. Ba-Abbad, A. W. Mohammad and A. Benamor, *Desalin. Water Treat.*, 2016, **57**, 7801–7811.
68 H. Zhang, J. Wu, J. Han, L. Wang, W. Zhang, H. Dong and Y. Wang, *Chem. Eng. J.*, 2020, **385**, 123764.
69 Y. Cao, S. Alsharif and A. S. El-Shafay, *Mater. Sci. Semicond. Process.*, 2022, **144**, 106569.
70 J. Ryu, S. Kim, H. I. Kim, E. H. Jo, Y. K. Kim, M. Kim and H. D. Jang, *Chem. Eng. J.*, 2015, **262**, 409–416.

71 K. Javed, M. Bilal, N. Abbas, S. Mahmood, T. Fazal, S. Iqbal and K. M. Alotaibi, *Microsc. Res. Tech.*, 2025, **88**, 1727–1738.
72 A. Mantilla, E. S. Benitez, I. M. Valenzuela, G. R. Ortiz, S. C. Díaz, L. L. Rojas, F. J. T. Morales and M. N. Magaña, *J. Photochem. Photobiol., A*, 2025, **459**, 116079.
73 Ö. Görmez, E. Yakar, B. Gözmen, B. Kayan and A. Khataee, *Chemosphere*, 2022, **288**, 132663.
74 Q. Han, M. Wang, F. Sun, B. Yu, Z. Dong, P. Li, J. Luo, M. Li, X. Jin and Z. Dai, *Environ. Res.*, 2023, **216**, 114601.
75 A. Saljooqi, T. Shamspur and A. Mostafavi, *Environ. Sci. Pollut. Res.*, 2021, **28**, 9146–9156.
76 G. Shukla, M. Rani and U. Shanker, *Inorg. Chem. Commun.*, 2025, **150**, 114733.
77 H. Dihingia and D. Tiwari, *Sep. Purif. Technol.*, 2023, **306**, 122641.
78 F. Liu, Q. Dong, C. Nie, Z. Li, B. Zhang, P. Han, W. Yang and M. Tong, *Chem. Eng. J.*, 2022, **430**, 132833.
79 J. Lai, X. Jiang, M. Zhao, S. Cui, J. Yang and Y. Li, *Appl. Catal. B*, 2021, **298**, 120622.
80 P. Xu, P. Wang, Q. Wang, R. Wei, Y. Li, Y. Xin, T. Zheng, L. Hu, X. Wang and G. Zhang, *J. Hazard. Mater.*, 2021, **403**, 124011.
81 J. Shen, A. Shi, J. Lu, X. Lu, H. Zhang and Z. Jiang, *Environ. Pollut.*, 2023, **323**, 121186.
82 P. Banerjee, E. Kemmler, M. Dunkel and R. Preissner, *Nucleic Acids Res.*, 2024, **52**, W513–W520.
83 G. Xiong, Z. Wu, J. Yi, L. Fu, Z. Yang, C. Hsieh, M. Yin, X. Zeng and C. Wu, *Nucleic Acids Res.*, 2021, **49**, W5–W14.
84 G. T. Ankley and D. L. Villeneuve, *Aquat. Toxicol.*, 2006, **78**, 91–102.
85 L. Guilhermino, T. Diamantino, M. C. Silva and A. M. Soares, *Ecotoxicol. Environ. Saf.*, 2000, **46**, 357–362.
86 J. Shen, A. Shi, J. Lu, X. Lu, H. Zhang and Z. Jiang, *Environ. Pollut.*, 2023, **323**, 121186.
87 Y. Quan, M. Liu, H. Wu, X. Tian, L. Dou, C. Ren and Z. Wang, *Appl. Surf. Sci.*, 2024, **664**, 160212.
88 Y. H. Azeez, R. O. Kareem, A. F. Qader, R. A. Omer and L. O. Ahmed, *Next Mater.*, 2024, **3**, 100184.
89 F. B. Shittu, A. Iqbal, M. N. Ahmad, M. R. Yusop, M. N. M. Ibrahim, S. Sabar, L. D. Wilson and D. H. Y. Yanto, *RSC Adv.*, 2022, **12**, 10409–10423.
90 Y. Hu, Y. Jin, Y. Gao, M. Li, X. Wang, H. Ma and Y. N. Zhang, *Adv. Funct. Mater.*, 2025, **35**, 2414350.
91 H. Yu, Y. Zhang, L. Wang, Y. Tuo, S. Yan, J. Ma, X. Zhang, Y. Shen, H. Guo and L. Han, *RSC Adv.*, 2024, **14**, 1854–1865.
92 C. Liu, M. Yue, L. Liu, Y. Rui and W. Cui, *RSC Adv.*, 2018, **8**, 22402.
93 R. Vaithiyanathan, K. Shanmugaraj, T. Kanagaraj, V. Manikandan, S. Singh, S. Dixit, M. S. A. J. Bosco, Y. Y. Li and P. S. M. Kumar, *Sep. Purif. Technol.*, 2025, **332**, 133389.
94 Y. Wang, S. Xue, Y. Liao, Q. Lu, H. Wang, C. Zhao, N. Tang and F. Du, *ACS Appl. Nano Mater.*, 2024, **7**, 3188–3198.
95 F. P. Hu, P. Zhan, L. Long, J. Zhu, G. Xu and X. Peng, *Chemosphere*, 2022, **293**, 133455.
96 N. P. de Moraes, R. B. Valim, R. S. Rocha, M. L. C. P. da Silva, T. M. B. Campos, G. P. Thim and L. A. Rodrigues, *Colloids Surf., A*, 2020, **584**, 124034.
97 A. Uddin, M. Bilal, J. Qian, M. Akram and Q. He, *Sep. Purif. Technol.*, 2025, **332**, 133420.